JGR Solid Earth

RESEARCH ARTICLE
10.1029/2019JB018002

Special Section:
Physical Properties of Rocks, Friction and Fracturing: The Walsh Volume

Stabilizing Effect of High Pore Fluid Pressure on Slip Behaviors of Gouge-bearing Faults

Tiange Xing[1], Wenlu Zhu[1], Melodie French[1,2], and Ben Belzer[1,2]

[1]Department of Geology, University of Maryland, College Park, MD, USA, [2]Department of Earth, Environmental and Planetary Sciences, Rice University, Houston, TX, USA

Key Points:
- Increasing pore fluid pressure leads to an apparent stronger velocity strengthening slip behavior in gouge-bearing experimental faults
- The net pore volume reduction (compaction) diminishes under high pore pressure conditions, implying an increasing dilation component
- Local dilatant hardening can explain the observed stabilizing effect of high pore pressure on frictional behaviors

Supporting Information:
- Supporting Information S1

Correspondence to:
T. Xing,
tiange@umd.edu

Citation:
Xing, T., Zhu, W., French, M., & Belzer, B. (2019). Stabilizing effect of high pore fluid pressure on slip behaviors of Gouge-bearing faults. *Journal of Geophysical Research: Solid Earth*, *124*, 9526–9545. https://doi-org.proxy-um.researchport.umd.edu/10.1029/2019JB018002

Received 9 MAY 2019
Accepted 22 AUG 2019
Accepted article online 29 AUG 2019
Published online 9 SEP 2019

Abstract We conducted experiments to investigate the influence of pore fluid pressure on the frictional strength and slip behavior of gouge bearing faults. Saw cut porous sandstone samples with a layer of gouge powders placed between the precut surfaces were deformed in the conventional triaxial loading configuration. A series of velocity-step tests were performed to measure the response of the friction coefficient to variations in sliding velocity. Pore volume changes were monitored during shearing of the gouge. Our results demonstrate that under constant effective pressure, increasing pore pressure stabilizes the frictional slip of faults with all four gouge materials including antigorite, olivine, quartz, and chrysotile. The stabilizing effect is the strongest in antigorite gouge, which shows an evolution of friction parameters from velocity-weakening toward velocity-strengthening behavior with increasing pore pressure. Experiments with controlled pore volume show that the pore volume reduction diminishes under high pore fluid pressures, implying an increasing dilation component at these conditions. The dilatant hardening mechanism can explain the observed strengthening. These results provide a possible explanation to the observed spatial correlation between slow slip events and high pore pressure in many subduction zones.

Plain Language Summary Elevated pore fluid pressures are often detected in regions where slow slip events occur. We conducted deformation experiments to investigate the effect of pore pressure on slip behaviors of gouge-bearing faults. Common minerals found at subduction interface, for example, antigorite, chrysotile, olivine, and quartz were used as gouge materials. We found that high pore pressure stabilizes the frictional slip of faults with all four gouge materials. In particular, antigorite-bearing faults exhibit velocity-weakening to velocity-strengthening slip behaviors as pore pressures increase. Furthermore, an increasing amount of pore volume dilation is accompanied by stronger stabilizing effect, consistent with the dilatant hardening model. This study provides new physical understanding of the observed spatial correlation between slow slip events and high pore pressure in many subduction zones.

1. Introduction

Geophysical observations reveal a variety of slip behaviors along the subduction interface, including seismogenic slip, slow slip, and aseismic creep. Compared to typical earthquakes, slow slip events have slower slip rates and smaller stress drops, and they generally lack high frequency seismic radiation (Peng & Gomberg, 2010). Slow slip events are observed at both the updip and downdip limits of subduction seismogenic zones, often in regions inferred to have elevated pore fluid pressures (Figure 1). For instance, evidence for the near-lithostatic pore fluid pressure occurs in regions of slow slip at the Nankai Trough and Cascadia (e.g., Kodaira et al., 2004; Peacock et al., 2011; Shelly et al., 2006). At the Hikurangi margin, regions inferred to have low fluid content are associated with seismicity while regions showing evidence of fluid overpressure correlates with aseismic creep (Heise et al., 2013, 2017). Together, these observations suggest that high pore fluid pressures may promote slow slip behaviors.

The mechanical effect of pore fluid pressure on fault slip is usually quantified with the law of effective stress, which states that the "effective" normal stress, $\sigma_n^{'}$, is equal to the total normal stress, σ_n, minus the pore fluid pressure, P_f, ($\sigma_n^{'} = \sigma_n - \alpha P_f$, where α is ~1 for brittle deformation; e.g., Terzaghi, 1943). Assuming a Coulomb-Amontons friction law, slip occurs when the shear stress along the fault, τ, reaches a critical value, $\tau_c = \mu(\sigma_n - P_f)$, where μ ($0.6 \leq \mu \leq 0.85$ for most rocks) is the coefficient of sliding friction (Byerlee, 1978). Thus, higher pore fluid pressure reduces the effective normal stress and causes the fault to slip at a lower shear stress. However, this stress threshold model of fault slip does not predict whether slip induced by high pore pressure is seismogenic or aseismic.

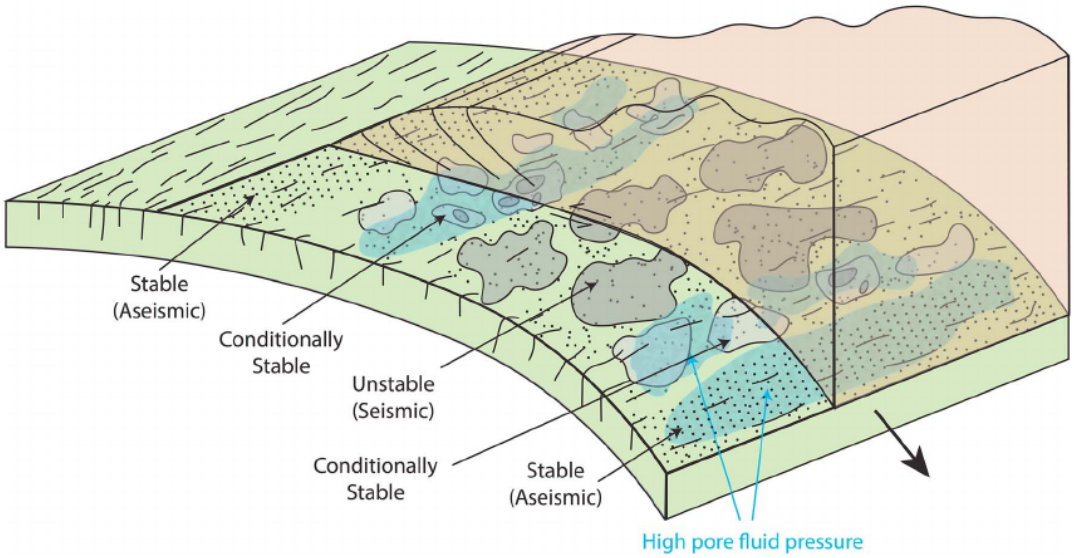

Figure 1. Illustration of the distribution of slip behavior within the subduction zone. A variety of slip behaviors are documented along subduction interface, and high pore fluid pressures have been correlated with the occurrence of transitional slip behaviors (modified from Bilek & Lay, 2002).

Models of fault slip stability have been derived from rate-and-state constitutive relations for frictional sliding. The difference between the empirical frictional parameters a and b represents the steady state velocity dependence of the frictional strength (e.g., Dieterich, 1979a; Ruina, 1983). A negative velocity dependence factor (a-b) describes fault weakening with increasing sliding velocity and such a system has the potential for dynamic runaway (Gu et al., 1984). A positive (a-b) fault strengthening with increasing sliding velocity, which results in stable sliding. It is proposed that slow slip events may arise from faults that are nearly velocity neutral, that is, at (a-b)~0 (e.g., Rubin, 2008) or when the effective pressure is low (e.g., Leeman et al., 2016). A more complete representation of the stability of frictional sliding can be described by a parameter called "the critical stiffness," k_c (Rice & Ruina, 1983):

$$k_c = \frac{-(a-b)\sigma_n'}{D_c} \tag{1}$$

where D_c is the characteristic slip weakening distance.

In this model, derived assuming constant σ_n', slip can accelerate to instability when k_c is greater than the system stiffness, k (Gu et al., 1984; Rice & Ruina, 1983). Thus, instability is favored for larger values of $-(a\text{-}b)$ and σ_n', and smaller values of D_c. As a result, any effect that pore fluid pressure has on these three parameters may stabilize or destabilize fault slip, depending on the sign and magnitude of the effect. Previous studies on the influence of high pore fluid pressure on these parameters have shown competing effects on fault stability.

Several experimental studies have investigated the role that P_f has on fault stability with different results (French et al., 2016; Ikari et al., 2009; Rutter & Hackston, 2017). For instance, Sawai et al. (2016) demonstrate that decreasing effective pressure (σ_n') causes a transition from stable to unstable slip behavior in blueschist samples. Ougier-Simonin and Zhu (2013, 2015) also observed that shear localization in porous rocks could become unstable by decreasing effective pressure as pore pressure increases during the post failure stage of faulting. In addition, French et al. (2016) and Scuderi et al. (2017) show that fluid pressurization can overcome velocity-strengthening friction to result in accelerated fault slip. On the other hand, slow slip events may arise or when the effective pressure is low (e.g., Leeman et al., 2016), and the low σ_n' associated with high pore fluid pressure is expected to stabilize slip. The apparent disagreements in whether high pore pressure enhances or impedes unstable slip could be due to the different rock materials tested.

In addition to the effects of pore fluid pressure on rate and state friction parameters, pore fluid pressure may have an effect on fault constitutive behavior that is not represented by this framework. For example, den Hartog and Spiers (2013) reported an increase in *(a-b)* in sheared gouge mixtures of quartz and illite with increasing pore fluid pressure at constant effective pressure. French and Zhu (2017) showed that at the same effective pressure, high pore fluid pressure reduced the rate of fault propagation in intact serpentinite and caused a transition from dynamic to quasi-stable faulting (French & Zhu, 2017). This stabilizing effect of high pore pressure has been explained by the dilatant hardening mechanism where the growth of cracks during brittle deformation leads to an increase in pore space, causing the pore pressure to drop and the local effective stress to rise, making it harder for cracks to grow. As such, dilatancy in a fluid-saturated rocks stabilizes fault propagation and strengthens the bulk rock (Brace & Bombolakis, 1963; Frank, 1965; Rice, 1975; Rudnicki & Chen, 1988).

Here we focus on the role that pore fluid pressure plays on controlling the rate and state frictional parameters of a rock *(a-b)*. The rate dependence *(a-b)* is controlled by a variety of factors, including mineralogy (e.g., Moore & Lockner, 2011), porosity (Blanpied et al., 1995; Takahashi et al., 2011), strain rate (French et al., 2015; Goldsby & Tullis, 2002; Niemeijer et al., 2010; Rabinowicz, 1958), temperature (Chernak & Hirth, 2010; Chester, 1994; Chester & Higgs, 1992; Lockner et al., 1986), and effective pressure (Carpenter et al., 2016; Morrow et al., 1992; Niemeijer & Collettini, 2013; Sawai et al., 2016). However, the effect of pore fluid pressure on *(a-b)* has not been distinguished from effects of $\bar{\sigma_n}$ on *(a-b)*.

In this study, we investigated whether the strengthening effect of high pore pressure stands true for frictional slip along gouge-bearing experimental faults. Phyllosilicate-rich rocks are common along seismogenic faults and plate boundaries. The slow slip events have also been repeatedly observed in phyllosilicate bearing seismogenic faults (e.g., Shelly, 2010). The frictional behavior of serpentines is, therefore, thought to have a great influence on the behavior of faults that exhibit diverse slip modes (Okazaki & Katayama, 2015; Reinen et al., 1994; Takahashi et al., 2011). Here we studied phyllosilicate gouges, antigorite, and chrysotile. For comparison, we also studied olivine and quartz gouges. We conducted a series of frictional sliding experiments with constant effective pressure but different pore fluid pressures to discern the effect of pore fluid pressure alone on the frictional properties of gouge. A series of velocity-stepping tests were performed to measure the response of friction coefficient to variations of sliding velocity; we measured the rate and state frictional parameters (*a-b*) and characteristic displacement D_c to quantify the effects of pore fluid pressure on slip stability. We also performed microstructural observations to constrain the deformation processes that lead to the observed mechanical behavior. Our goal is to gain a better understanding of the effect of high pore pressure on frictional behavior, which has important implications on the occurrence of different types of slip events in subduction zones.

2. Experimental Procedures

In this study, we investigate two serpentine gouge powders, the Verde Antique antigorite and Zimbabwe chrysotile. Together with olivine and quartz, San Carlos olivine and quartz powders from U.S. Silica, respectively, our samples include common minerals present along plate boundary faults. The modal mineralogy of the antigorite, chrysotile, and olivine gouges are quantified using X-ray powder diffraction (see supporting information Figures S6–S8). The Verde Antique antigorite is composed of 90.8% antigorite with 9.2% iron oxides. The Zimbabwe chrysotile is composed of 42.8% lizardite, 41.8% chrysotile, and 15.5% brucite. The San Carlos olivine is ~100% olivine.

For each experiment, a layer of fine-grained gouge (<150 μm) composed of 2 g of dry serpentine powders was placed along a 30° saw cut surface in a cylindrical porous sandstone shearing block (25.4 mm in diameter and 50.8 mm in height; see Figure 2). We varied the mass of the powders in order to maintain a consistent gouge thickness of ~1 mm (~2 g for serpentines, ~2.6 g for olivine, and ~2.1 g for quartz), which is necessary because the density differences between serpentine (~2.52 g/cm^3), olivine (3.27 g/cm^3), and quartz (2.65 g/cm^3). We added a few drops of distilled water into the dry powder to spread the gouge evenly over the saw cut surface and to saturate the gouge layer. The sandstone shearing blocks were made of Berea sandstone which has a porosity of ~20% and permeability ~5×10^{-13} m^2 (Zhu & Wong, 1997), and the saw cut surface was ground with 120-grit diamond wheel to ensure a consistent surface property.

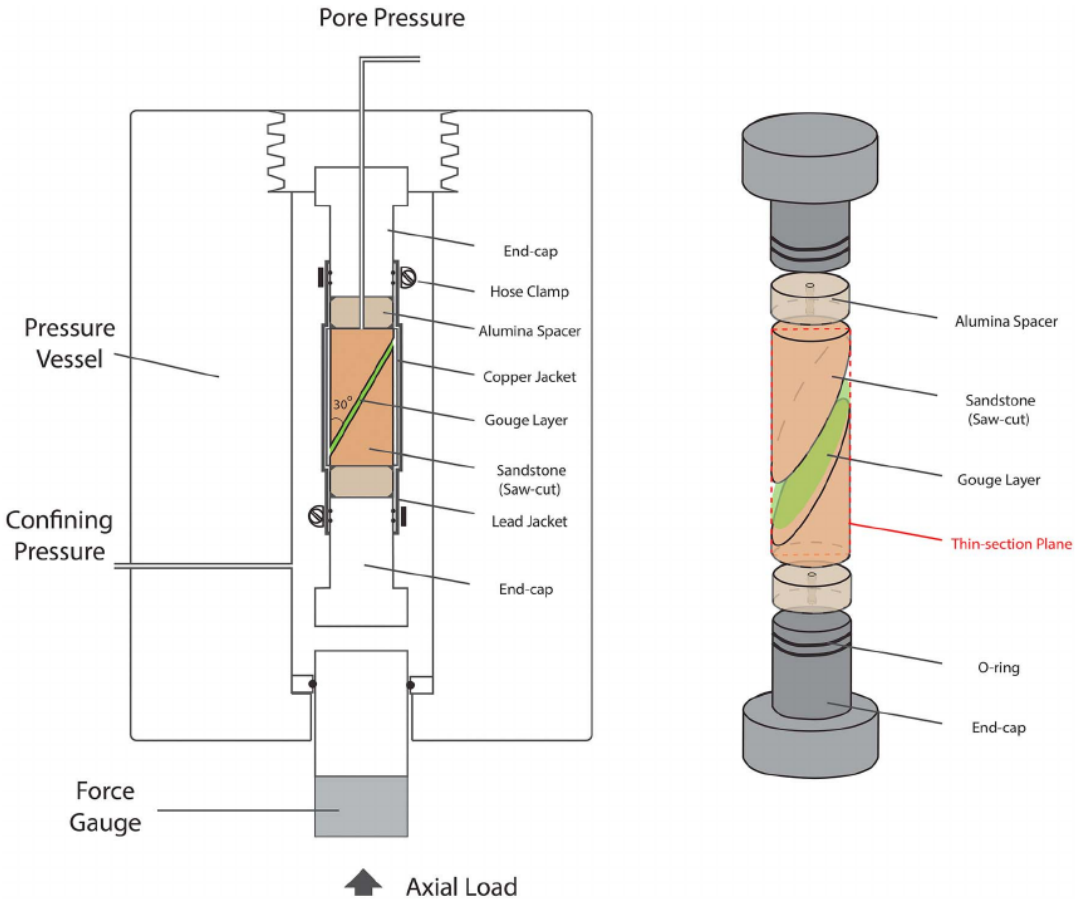

Figure 2. Sample and apparatus configuration. A traditional triaxial deformation apparatus is used in this study. The confining pressure and pore pressure are controlled individually through external servo-controlled intensifiers. Thin sections of deformed samples are made along the plane marked by the red dashed line. The equipment configuration is for illustration only and is not to scale.

The gouge and forcing blocks were jacketed in a 0.05-mm thick copper foil; the sample and two alumina spacers were then inserted into a 1.27-mm thick lead tube with an inner diameter of ~53 mm. The lead jacket was then sealed by hose-clamps and o-rings to the endcaps (see Figure 2). Pore fluid access to the sample was provided by small centric holes in the alumina spacers and end caps. Argon gas and deionized water were used as the confining medium and pore fluid respectively.

Before each experiment, the saturated sample was first brought to a confining pressure (P_c) of 20 MPa and allowed to precompact for ~15 hr. A pore pressure (P_f) of 10 MPa was then applied to purge air bubbles from the system. After that, the confining and pore pressures were changed to the desired experimental conditions for the friction experiments. Gouge layers were sheared at an effective pressure (P_c-P_f) of either 30 or 70 MPa (Table 1); for experiments conducted at 70-MPa effective pressure (P_c-P_f), the pore pressures ranged from 5 to 60 MPa, and for experiments conducted at 30-MPa effective pressure, the pore pressures ranged from 10 to 90 MPa. Confining pressure was determined to achieve the desired effective pressure and all experiments were conducted at room temperature.

Two series of experiments were conducted. In one series, the pore pressure was kept constant under servo control (referred to as constant pore pressure, CPP, experiments). During shearing of the gouge, changes in pore volume were measured from displacement of a linear variable differential transformer (LVDT) affixed to the pore pressure intensifier piston. Velocity stepping tests were performed to obtain rate-and-state frictional parameters during CPP tests. In the other series of experiments, the sample was initially loaded at

Table 1
Summary of Experiments

CPP Experiments								
Gouge	P_c (MPa)	P_f (MPa)	P_c-P_f (MPa)	μ	σ_{yield} (MPa)	$(a\text{-}b)^+$	$(a\text{-}b)^-$	D_c (mm)
Atg^	75	5	70	0.57	157.8	−0.0042 ± 0.0010	−0.0044 ± 0.0020	0.1074 ± 0.0165
Atg^	100	30	70	0.58	155.1	−0.0025 ± 0.0010	−0.0030 ± 0.0016	0.1165 ± 0.0269
Atg^	130	60	70	0.60	151.1	−0.0015 ± 0.0010	−0.0035 ± 0.0007	0.1308 ± 0.0343
Ctl^	75	5	70	0.33	71.1	0.0072 ± 0.0015	0.0047 ± 0.0020	0.0223 ± 0.0100
Ctl^	100	30	70	0.33	71.5	0.0069 ± 0.0017	0.0072 ± 0.0010	0.0338 ± 0.0260
Ctl^	130	60	70	0.33	68.1	0.0072 ± 0.0015	0.0069 ± 0.0006	0.0262 ± 0.0066
Ol^	75	5	70	0.69	151.0	0.0059 ± 0.0009	0.0050 ± 0.0009	0.0373 ± 0.0432
Ol^	100	30	70	0.69	148.0	0.0064 ± 0.0005	0.0057 ± 0.0006	0.0365 ± 0.0125
Ol^	130	60	70	0.65	145.9	0.0063 ± 0.0005	0.0054 ± 0.0005	0.0426 ± 0.0108
Qz^	75	5	70	0.68	163.6	0.0041 ± 0.0005	0.0025 ± 0.0003	0.0567 ± 0.0247
Qz^	100	30	70	0.68	161.4	0.0042 ± 0.0003	0.0026 ± 0.0006	0.0559 ± 0.0184
Qz^	130	60	70	0.69	159.2	0.0043 ± 0.0006	0.0032 ± 0.0009	0.0604 ± 0.0210
Atg^	40	10	30	0.65	69.8	0.0068 ± 0.0020	0.0070 ± 0.0019	0.0289 ± 0.0070
Atg^	60	30	30	0.72	76.5	0.0073 ± 0.0018	0.0056 ± 0.0015	0.0265 ± 0.0054
Atg^	90	60	30	0.64	64.7	0.0033 ± 0.0181	0.0055 ± 0.0045	0.0235 ± 0.0058
Atg^	120	90	30	0.72	76.4	0.0083 ± 0.0023	0.0094 ± 0.0008	0.0236 ± 0.0075
CPV Experiments								
Gouge	P_c (MPa)	P_f (MPa)	P_c-P_f (MPa)	μ	σ_{yield} (MPa)			
Atg*	40	10	30	0.737	63.7			
Atg*	60	30	30	0.718	70.0			
Atg*	90	60	30	0.629	62.2			
Atg*	120	90	30	0.678	66.4			
Ctl*	40	10	30	0.445	32.0			
Ctl*	120	90	30	0.434	28.5			
Ol*	40	10	30	0.764	70.4			
Ol*	90	60	30	0.742	66.2			
Ol*	120	90	30	0.747	66.8			
Qz*	40	10	30	0.721	73.9			
Qz*	120	90	30	0.732	73.6			

Note. Atg = Antigorite; Ctl = Chrysotile; Ol = Olivine; Qz = quartz; (^) = tests under CPP; (*) = tests under CPV; ($^+$) = velocity increasing steps; ($^-$) = velocity decreasing steps. The reported values of *(a-b)* are the average and standard deviation for all velocity steps in an experiment. CPP = constant pore pressure; CPV = controlled pore volume experiment.

constant pore pressure, and once sliding occurs, pore volume was held approximately constant by locking the piston of the pore pressure intensifier (referred to as constant pore volume, CPV, experiments). During the CPV tests, the tendency for the samples to dilate or compact resulted in a decrease or increase in P_f, which was monitored. We unlocked the pore pressure intensifier intermittently to keep the pore fluid pressure within ~5 MPa of the target pressure. In reality, the total fluid mass in the sample and intensifier was held constant in these experiments, and the total volume varied slightly as the pores contract or dilate. Given the compressibility of water ($\sim 4 \times 10^{-4}$ MPa^{-1}), a 5 MPa increase in pressure is equivalent to a water volume reduction of ~0.03 ml for a total water volume (sample + intensifier) of 14 ml. Assuming that all pore volume change is due to gouge deformation, this corresponds to a gouge volume reduction of ~3.4%. Because of the changing pore pressure during CPV tests, measurements of (*a-b*) and D_c showed large variation due to pressure fluctuations. Thus, the (*a-b*) and D_c from CPV experiments were not used to discuss the slip behavior.

Samples were deformed at a constant axial displacement rate (loading velocity) of 0.5 μm/s. For each deformation test, once slip along the saw cut surface occurred (at ~1.5-mm axial displacement), the axial displacement velocity was stepped in increments between 0.1 and 5 μm/s (0.12 and 5.77 μm/s sliding velocity; see Table 1). To ensure a drained condition of the gouge, the sliding velocity was limited to between 0.1 and 1 μm/s during the CPP experiments. Following each velocity step, we allowed 0.5-mm axial displacement to achieve a new steady state for reliable measurement of rate and state friction parameters. The axial displacement was measured by a LVDT affixed to the axial piston. An external force gauge was mounted at the

piston outside the vessel from which the axial load (σ_1) was measured (see Figure 2). The differential stress ($\Delta\sigma = \sigma_1 - P_c$) was calculated from the axial load and corrected for o-ring seal friction due to its placement outside of the pressure vesselx (Appendix A1).

The friction coefficient μ (shear stress τ normalized by the effective normal stress ($\sigma_n - P_f$) on the fault plane) is calculated from differential stress ($\Delta\sigma$) from the following equation:

$$\mu = \frac{\tau}{\sigma_n - P_f} = \frac{0.5\Delta\sigma\sin(2\phi)}{\Delta\sigma\sin^2(\phi) + P_c - P_f} = \frac{0.5\Delta\sigma\sin(2\phi)}{0.5\Delta\sigma(1-\cos(2\phi))} + P_c - P_f \quad (2)$$

where ϕ is the angle between the gouge layer and the axial load σ_1 (30°). The shear and normal stresses are corrected for decreasing area of contact along the sawcut with increasing displacement (Appendix A2).

The velocity dependence factor (a-b) and characteristic displacement (D_c) are determined from the measurements using the rate- and state-dependent friction model (Dieterich, 1979; Ruina, 1983). Calculation of the velocity dependence factor (a-b) and the measurement of D_c are discussed in detail in the Appendix A3.

The deformed samples were epoxy impregnated after the deformation and were cut perpendicular to the shear plane and parallel to the slip vector (see Figure 2). Thin sections of antigorite and olivine gouges were made after the experiments and were used for microstructural analyses.

3. Results

3.1. Frictional Strength and Friction Coefficient From CPP Experiments

The yield strengths of the samples having the same composition and deformed under the same effective pressure (P_c-P_f) vary less than 5% (see supporting information Figure S1), indicating that the mechanical strength obeys the effective pressure law, with effective pressure of (P_c-P_f) and α-value close to 1. Both serpentine gouges exhibit strain hardening to a peak strength followed by subsequent strain weakening to a steady state strength (Figure 3a). In contrast, olivine and quartz gouges both exhibit strain hardening until a steady state strength is achieved. These results are consistent with previous experimental studies on gouges rich in phyllosilicates and other silicate minerals (e.g., Den Hartog et al., 2014; Escartín et al., 1997; Proctor et al., 2014).

Like the yield strength, the friction coefficient of a given gouge composition shows no obvious correlations with pore pressure magnitude (Figure 3a). The two serpentines have lower friction coefficients than those of the olivine and quartz. Chrysotile has the lowest friction coefficient of ~0.33, and the friction coefficient of antigorite shows a range from ~0.57 to 0.60. These observations are consistent with previously reported strengths of serpentine minerals (e.g., Moore et al., 1996, 2004; Proctor et al., 2014). The friction coefficients of olivine and quartz show a range from ~0.65 to 0.69 and are in agreement with previous observations for these minerals as well (e.g., Dieterich & Conrad, 1984; Takahashi et al., 2011).

3.2. Frictional Velocity Dependence From CPP Experiments

The rate and state frictional parameter a for all gouge materials does not vary measurably between gouges of different compositions (Figure 3b). However, the value of b is measurably higher for antigorite than for quartz, while olivine and chrysotile show near 0 values for parameter b (Figure 3b). In this study, the velocity dependence factors (a-b) is much better constrained from the experimental data than the parameters a and b individually (Verberne et al., 2010). Therefore, only the steady state velocity dependence (a-b) is discussed in further detail (Table 1).

Among the gouges studied here, only antigorite shows velocity-weakening behavior, (a-b) < 0 in slip response at the testing conditions (Figure 3b), whereas olivine, quartz, and chrysotile gouges all exhibit velocity-strengthening behavior, (a-b) > 0. Chrysotile, which has the lowest friction coefficient, also shows the most positive (a-b) among all the compositions tested. This is consistent with the result of Ikari et al. (2011) that gouges having a friction coefficient of $\mu < 0.5$ tend to exhibit stable sliding behavior.

An asymmetric frictional response to increasing and decreasing velocity steps is observed in (a-b) values (see supporting information Figure S2). Specifically, the values of (a-b) determined from decreasing velocity steps (1 to 0.1 μm/s; Table 2) are lower than those from increasing velocity steps (0.1 to 1 μm/s; Table 2). The

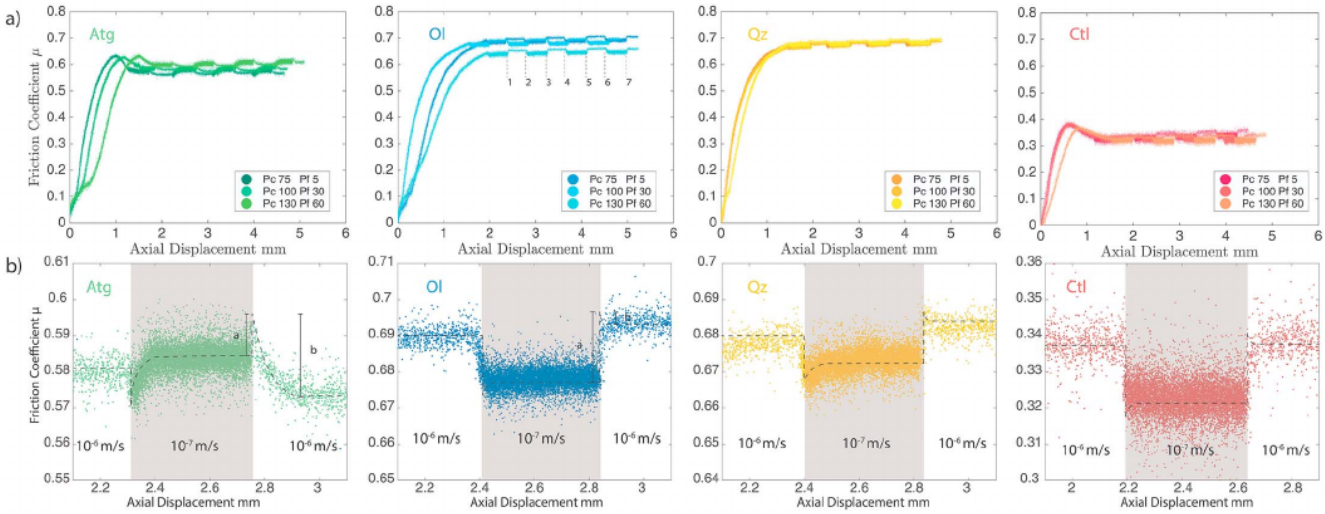

Figure 3. (a) The friction coefficient of antigorite (green), olivine (blue), quartz (yellow), and chrysotile (red) for constant pore pressure experiments. The velocity steps are marked in the plot for olivine friction and same sequence was used in all experiments. (b) Detailed plots showing velocity steps from experiments conducted at 100 MPa P_c and 30 MPa P_f. Steps from higher (1 μm/s, white) to lower (0.1 μm/s, shaded) velocities and back are shown.

asymmetry is more significant in olivine and quartz friction experiments. Rathbun and Marone (2013) reported that, D_c is larger in velocity decrease steps than the velocity increase steps and argue that this was due to shear localization and changes in shear fabric in fault gouge. The pore structure evolution can be affected by the step direction. This may cause the D_c and (a-b) to show asymmetry between velocity increase and decrease steps. The asymmetry of friction parameters is also discussed by (Chen et al., 2017). These differences in shear localization and shear fabric may also affect the (a-b), leading to the asymmetry observed in our study. Due to this asymmetry, averaging (a-b) values from increasing and decreasing velocity steps exaggerates the apparent variability.

To better illustrate the effect of pore fluid pressure on (a-b), we compared results from velocity increase and decrease steps separately. The (a-b) values for each increasing velocity step (0.1 to 1 μm/s) is calculated and plotted against the pore pressure in Figure 4, and the results for decreasing velocity steps are given in the supporting information (Figure S3) The value of (a-b) increases with increasing pore pressure for all gouge composition, which records an apparent strengthening effect of increasing pore pressure on fault strength. The strengthening effect is greatest in antigorite, for which we observed an increase in (a-b) of ~5×10^{-5} MPa^{-1} with increasing pore pressure. This corresponds to ~1% of (a-b) per MPa increase in pore pressure. Olivine, quartz, and chrysotile show a smaller correlation between pore pressure and (a-b) compared to antigorite (Figure 5).

3.3. Characteristic Displacement From CPP Experiments

The characteristic displacement (D_c) of each step is reported for all materials at conditions of 100-MPa confining pressure and 30-MPa pore pressure (Figure 6a). The uncertainties in the absolute D_c values could be considerable due to the specific machine configuration. Nevertheless, the relative values of D_c for different

Table 2
Axial Displacement Rate for the Step Tests During Each Experiment

Step #	1	2	3	4	5	6	7
Velocity Steps (μm/s)	0.1 to 1($^+$)	1 to 0.1($^-$)	0.1 to 1($^+$)	1 to 0.1($^-$)	0.1 to 1($^+$)	1 to 0.1($^-$) for CPP 1 to 5 ($^+$) for CPV	0.1 to 1 ($^+$) for CPP 5 to 1 ($^-$) for CPV
Axial Displacement (mm)	~0.5	~0.5	~0.5	~0.5	~0.5	~0.5	~0.5

Note. For steps 6 and 7, the axial displacement rate is 1 to 0.1 and 0.1 to 1 μm/s for CPP experiments and 1 to 5 and 5 to 1 μm/s for CPV experiments. ($^+$) = velocity increasing steps; ($^-$) = velocity decreasing steps.

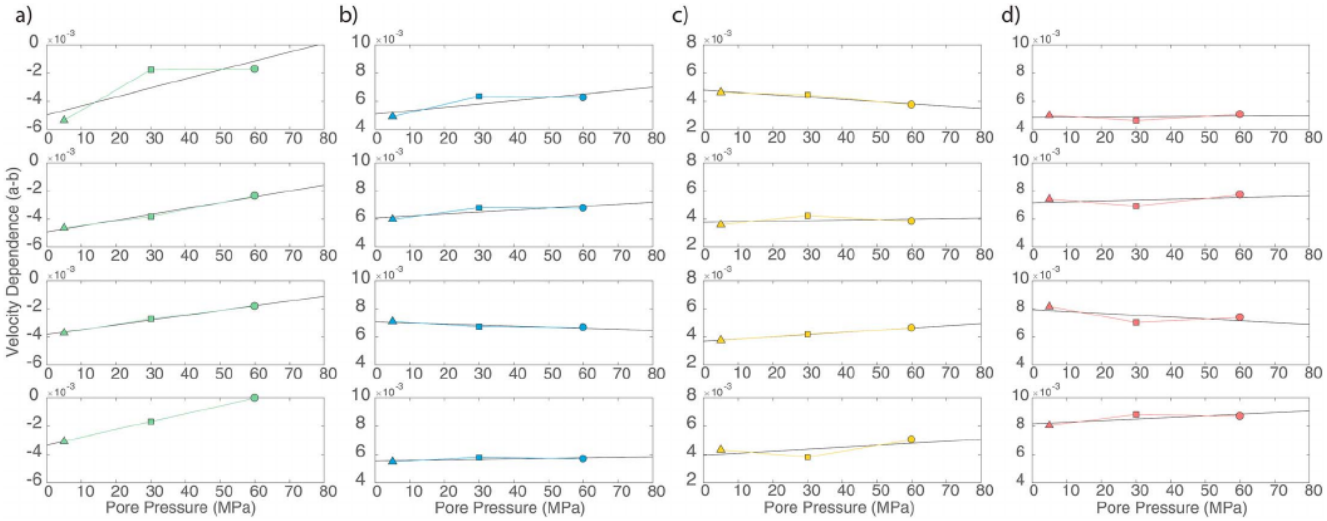

Figure 4. The correlation between velocity dependence factor (a-b) and pore pressure for (a) antigorite, (b) olivine, (c) quartz, and (d) chrysotile for velocity steps up from 0.1 to 1 μm/s in CPP experiments at effective pressure of 70 MPa. The strengthening rate of (a-b) from pore pressure is calculated based on the slope of the fitted line in the plot. The evolution in (a-b) with increasing pore pressure is generally positive, and greatest in antigorite.

gouges obtained at the same experimental conditions can be compared. D_c is the largest in antigorite compared to all other minerals; for antigorite, the average value of D_c is ~0.12 mm while olivine, quartz, and chrysotile all have an average D_c of ~0.05.

We also compared the value of D_c in antigorite at different pore pressures ranging from 5 to 60 MPa (Figure 6b). Notwithstanding some scattering, D_c is generally higher in experiments at pore pressures of

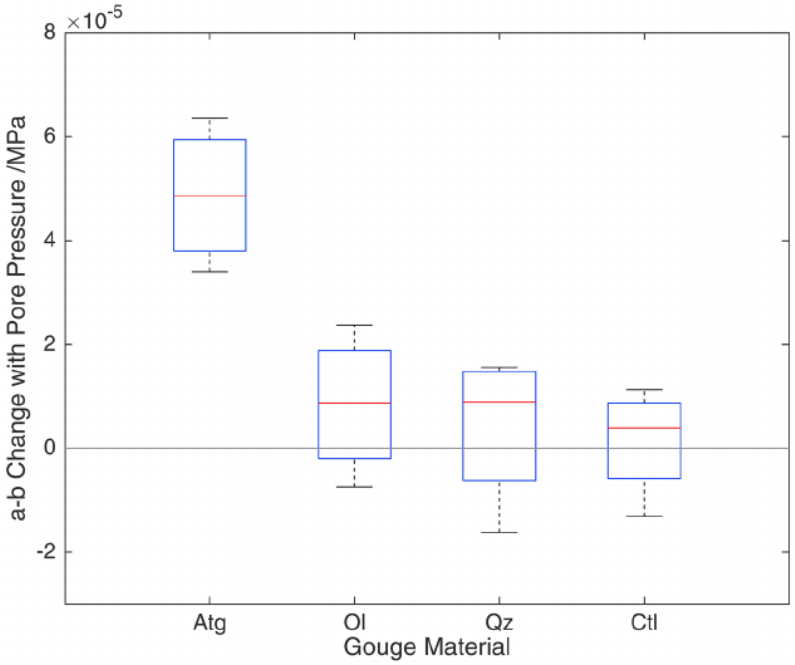

Figure 5. A box plot showing change in (a-b) with pore pressure (slope of the fitted lines in Figure 4). Only (a-b) from increasing velocity steps (0.1 to 1 μm/s) is presented in this plot.

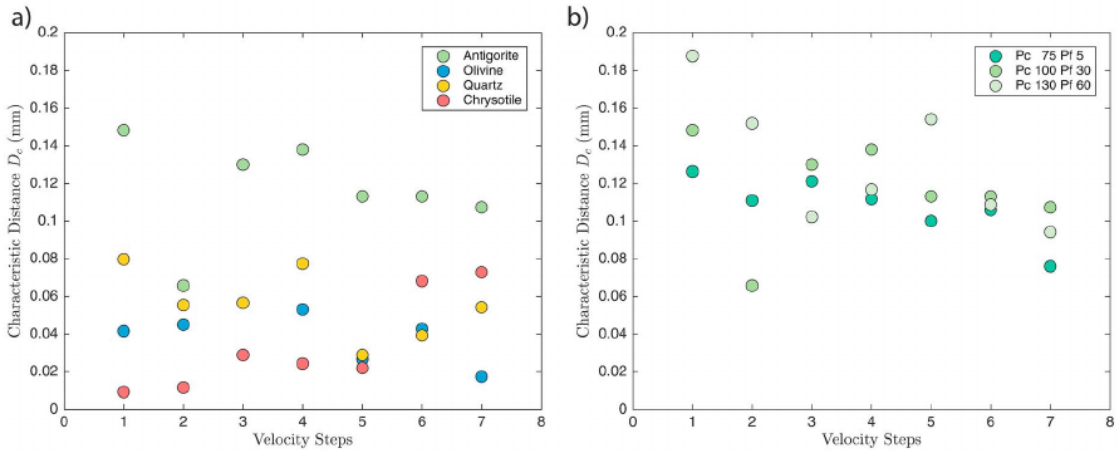

Figure 6. a) The characteristic displacement (D_c) for gouges shown for each velocity-step test. All experiments shown here are conducted at 100 MPa $P_c$and 30 MPa P_f; (b) Characteristic displacement (D_c) of antigorite in response to steps in slip velocity shown for 70-MPa effective pressure and different pore pressures.

30 or 60 MPa than those at 5 MPa. This suggests that higher pore pressure could cause an increase in the characteristic displacement.

3.4. Pore Volume Fluctuations From CPP Experiments

Before the start of deformation in each experiment, the pore volume of the P_f intensifier is adjusted to the same level. Thus, we can assume that the total pore volume in the sample and the system is similar among all experiments. For the data presentation, pore volume at the beginning of the deformation is neutralized to 0.

All experiments showed a net pore volume reduction (compaction) during frictional sliding (Figure 7). In addition, we observed transient fluctuations in the position of the pore pressure intensifier piston during slip, likely reflecting the responses of the servo control to sudden changes in pore volume. Figure 7 shows that the pore volume fluctuation (i.e., from −0.5 to 0.3 ml) becomes more frequent at higher pore pressures in antigorite gouge. Comparing quartz with antigorite, the amplitude of pore volume fluctuation (i.e., −0.2–0.1 ml) is smaller. Because the (a-b) shows a stronger correlation with pore pressure in antigorite than in quartz, the possible link between the pore volume fluctuation and the strengthening were investigated.

3.5. Pore Pressure Variations During CPV Experiments

In the CPV experiments (Table 2), samples deformed at an initial pore pressure less than 60 MPa show clear and repeatable increases in pore pressure when the intensifier is locked (Figure 8). In samples deformed at initial pore pressures greater than 60 MPa, however, little pore pressure variation was observed when the intensifier was locked.

During frictional sliding, processes that cause both local compaction (e.g., pore collapse) and dilation (e.g., fracturing) take place within the sample (e.g., Morrow & Byerlee, 1989). Competition between the compaction and dilation components determines the net (bulk) pore volume change. Our CPV data indicate that high pore pressure suppresses compactive processes and/or promotes dilatant processes relative to lower pore pressure conditions.

The pressurization rate during CPV tests is greater in samples deformed at low initial pore pressures than that at high pore pressures (Figures 8 and 9), and this decrease in pressurization rate with increasing pore pressure is observed in all materials (Figure 9). The antigorite shows the largest contrast in rate of pressurization between low and high pore pressure. The rate of pore fluid pressurization decreases with increasing slip velocity leading to a decrease in the contrast in pressurization rate between low and high pore pressure experiments at slip velocities greater than 1 μm/s (Figure 9).

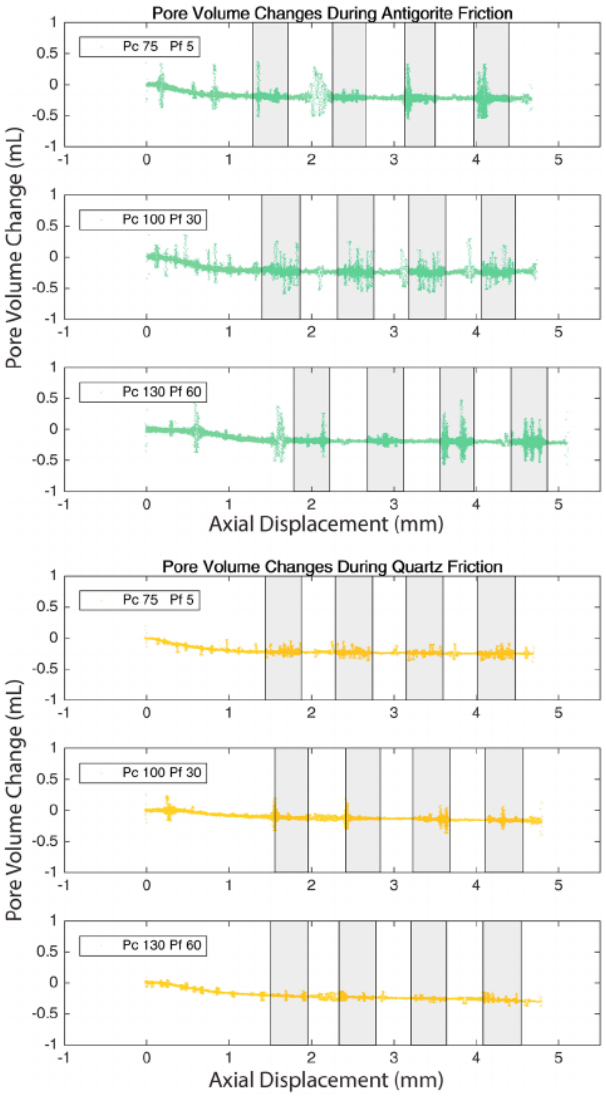

Figure 7. Pore volume changes of antigorite (green) and quartz (yellow) during deformation. The white and shaded areas show fast (1 μm/s) and slow (0.1 μm/s) slip velocity steps, respectively. Experiments were conducted at 70-MPa effective pressure. Compaction of the pore space is represented by negative pore volume change and dilation represented by positive pore volume change.

3.6. Microstructure of the Deformed Gouge

We observed Y fractures (Logan et al., 1992) in antigorite and olivine gouges deformed at all conditions (Figure 10). Both gouge compositions exhibit R_1 (Riedel) shear fractures at higher pore fluid pressure but not at lower pore pressure. In addition, gouges deformed at higher pore pressure have fewer large grains than those deformed at lower pore pressures despite the fact that they were deformed at the same effective pressure (70 MPa). This demonstrates that there is more extensive grain size reduction at higher pore pressure than at lower pore pressure in antigorite and olivine. The thickness of the zone of comminution where intense grain size reduction is observed also increases with increasing pore pressure at constant effective pressure indicating that strain is more distributed at high pore pressure conditions. The development of shear fracture and cracking during grain size reduction can all contribute to the pore volume dilation during deformation.

4. Discussion

4.1. Frictional Behavior Change With Increasing Pore Pressure

The friction coefficients of all gouges that we studied are consistent with previous studies which report that the serpentines are weaker than olivine and quartz (Beeler, 2007; Dieterich & Conrad, 1984; Takahashi et al., 2011) and that chrysotile is the weakest and promotes stable sliding at our experimental conditions (Ikari et al., 2011; Moore et al., 1996, 2004).

Calculations of the velocity dependence factor (a-b) demonstrate that higher pore pressures can cause an increase in (a-b), thereby stabilizing frictional slip. For instance, the smallest value of (a-b) measured for antigorite is -4.2×10^{-3} at 5-MPa pore pressure and 75-MPa confining pressure. If we extrapolated these results to 80-MPa pore pressure and 150-MPa confining pressure given the measured correlation between pore pressure and (a-b) ($\sim 5 \times 10^{-5}$ MPa^{-1}), then the relationship predicts a transition of the frictional behavior of antigorite from velocity weakening to velocity strengthening. This corresponds to a change in slip behavior from potential unstable to stable slip.

It is noted that with increasing slip rates, the pore fluid eventually becomes undrained. Under undrained conditions, the pore pressure measurements at the transducer do not reflect pore pressure changes within the gouge. However, at low slip rates, the gouge is considered as drained and the pore pressure measurements accurately track the pressure within the gouge. We calculated the diffusion time which describes the time for the fluid in the gouge to equilibrate after perturbations using the following equation:

$$t = \frac{h^2 \beta \eta}{2k} \tag{3}$$

where h is the diffusion length, β is the compressibility of the gouge, η is the viscosity of the fluid, and k is the permeability of the gouge. We adopt the compressibility value of 10^{-10} Pa^{-1} and fluid viscosity of 0.001 Pa·s base on Faulkner et al. (2018). We assume a gouge permeability of 10^{-20} m^2 (Faulkner & Rutter, 2003; Ikari et al., 2009; Morrow et al., 1984). The calculated diffusion time is ~1.25 s. The gouge compaction takes place at grain contact scale of ~1 μm. When slip rate is at 5 μm/s, the time scale for compaction is ~0.2 s. In this case, the gouge can be considered as undrained at the contact scale. While at slip rate of 1 μm/s or lower, the compaction takes place at a time scale of 1–10 s. Therefore, the gouge is drained at slip rate of 0.1 to 1 μm/s.

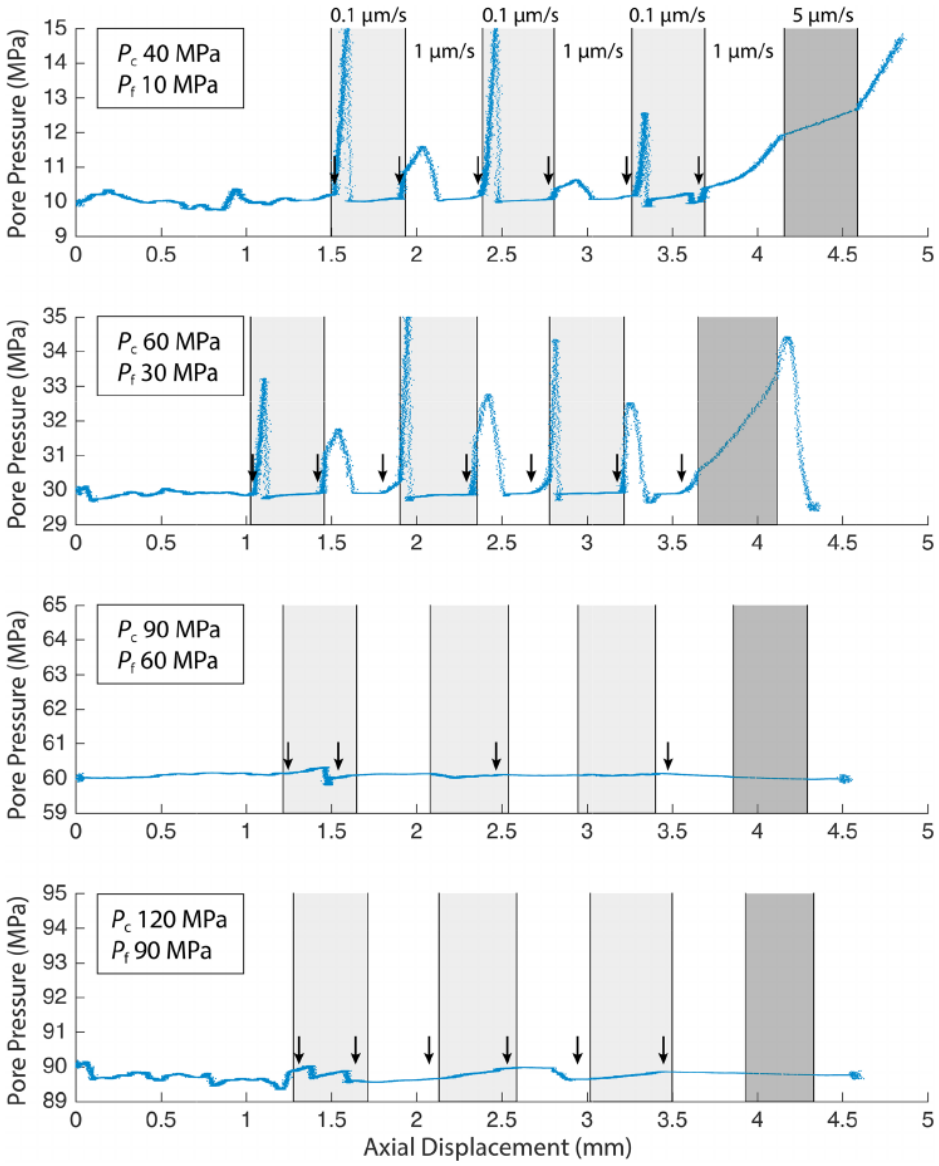

Figure 8. Pore pressure changes of antigorite gouge during constant pore volume experiments. The white and light grey areas show fast (1 μm/s) and slow (0.1 μm/s) slip velocity steps, respectively. The dark grey area represents a slip velocity of 5 μm/s. The black arrows mark the point at which the pore volume is fixed by locking the pore pressure intensifier. In order to maintain conditions comparable with the constant pore pressure tests, we prevented the pore pressure from varying more than 5 MPa from the initial conditions by regaining servo control of pore pressure intensifier.

4.2. Pore Volume Change During Shear

The increase in pore pressure during CPV experiments and the inverse correlation between pressurization rate and the magnitude of pore pressure cannot be explained by the dependence of water compressibility on pore pressure. Specifically, the compressibility of water (β) is described by the equation:

$$\beta = -\frac{1}{V_p}\left(\frac{\partial V_p}{\partial P}\right)_T \tag{4}$$

where V_p is the volume, P is the pore pressure, and T is the temperature. The compressibility of water with respect to pore pressure at room temperature. The compressibility of water decreases with increasing pore

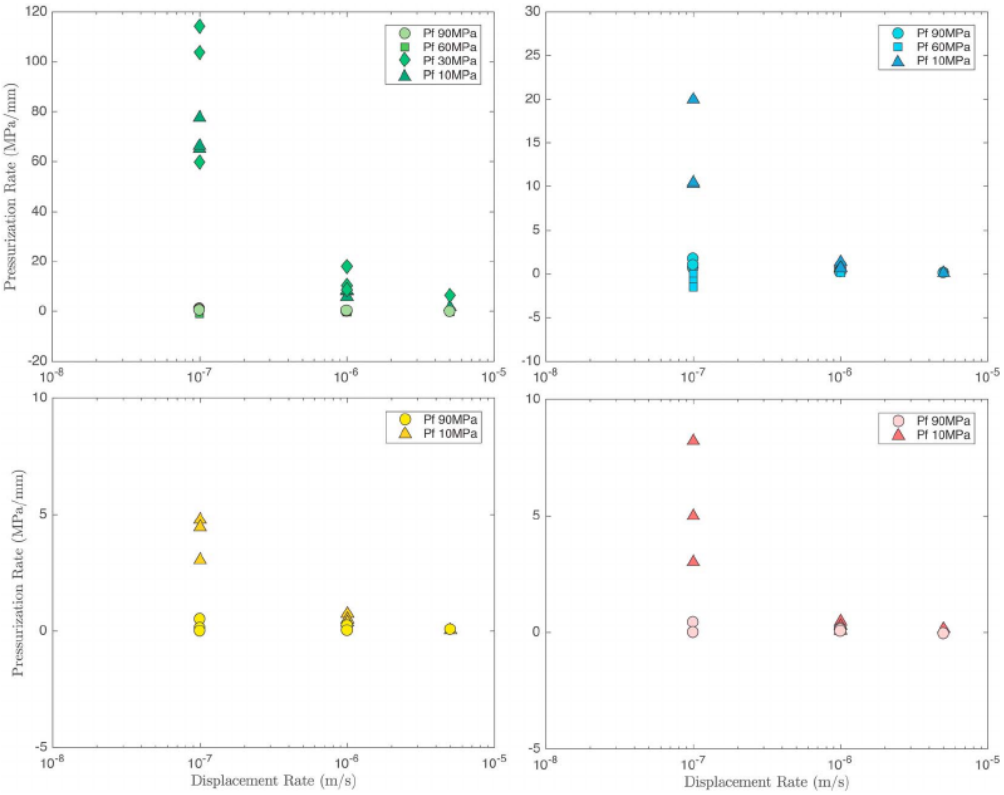

Figure 9. The pore fluid pressurization rate (with displacement) of antigorite (green), olivine (blue), quartz (yellow), and chrysotile (red), during constant pore volume experiments at different axial displacement rates. Experiments were conducted at effective pressure of 70 MPa. The fluid pressurization rate decreases with increasing pore pressure.

pressure from 4.41×10^{-4} MPa^{-1} at 10 MPa to 3.62×10^{-4} MPa^{-1} at 90 MPa at room temperature (Fine & Millero, 1973). This indicates that for the same change in pore volume, a larger change in pore pressure is expected at higher pore pressures, which is the opposite of our observations.

In our antigorite experiment from CPV, we observed a 5-MPa pore pressure increase over ~0.08 mm of axial displacement following a lock on the pore volume during the deformation, which corresponds to a pore fluid pressurization rate of ~74 MPa/mm. This 5-MPa increase in pore pressure is equivalent to a pore volume reduction of ~0.03 ml, assuming a total pore volume (sample + intensifier) of 14 ml. For a cylindrical sample of 25.4 mm in diameter and 50.8 mm in height, this correspond to a sample volume reduction of ~0.12%. Assuming that all pore volume change is due to gouge deformation. This would correspond to a gouge volume reduction of ~3.4%, assuming a gouge porosity of ~10%.Considering the change in water compressibility at the lowest and highest pore pressures that we studied, the same sample volume reduction that leads to a 5-MPa increase in pressure at 10-MPa pore pressure would cause a 5.9-MPa pore pressure increase at 90-MPa pore pressure. However, we do not observe a systematic increase in pressurization rate at 90 MPa. It follows that the pressure-dependent compressibility cannot explain the differences in pressurization rate at different pore pressure in our study. Thus, the decrease in pressurization rate with increasing pressure must reflect a decrease in the net pore compaction rate with increasing pressure.

Gouge deformation (granular flow) following a change in the slip velocity is a competition between pore volume compaction and dilation (e.g., Morrow & Byerlee, 1989). A decrease in the net compaction effect with increasing pore pressure could be resulted from a decrease in the compaction component or an increase in the dilation component associated with pore pressure increase. Change in the compaction component is a result of the variation in effective normal stress ($\sigma_n^{'} = \sigma_n - \alpha P_f$). The observed decrease in compaction with increasing pore pressure would require an α value higher than 1 which is not supported by our stress-

pMKO

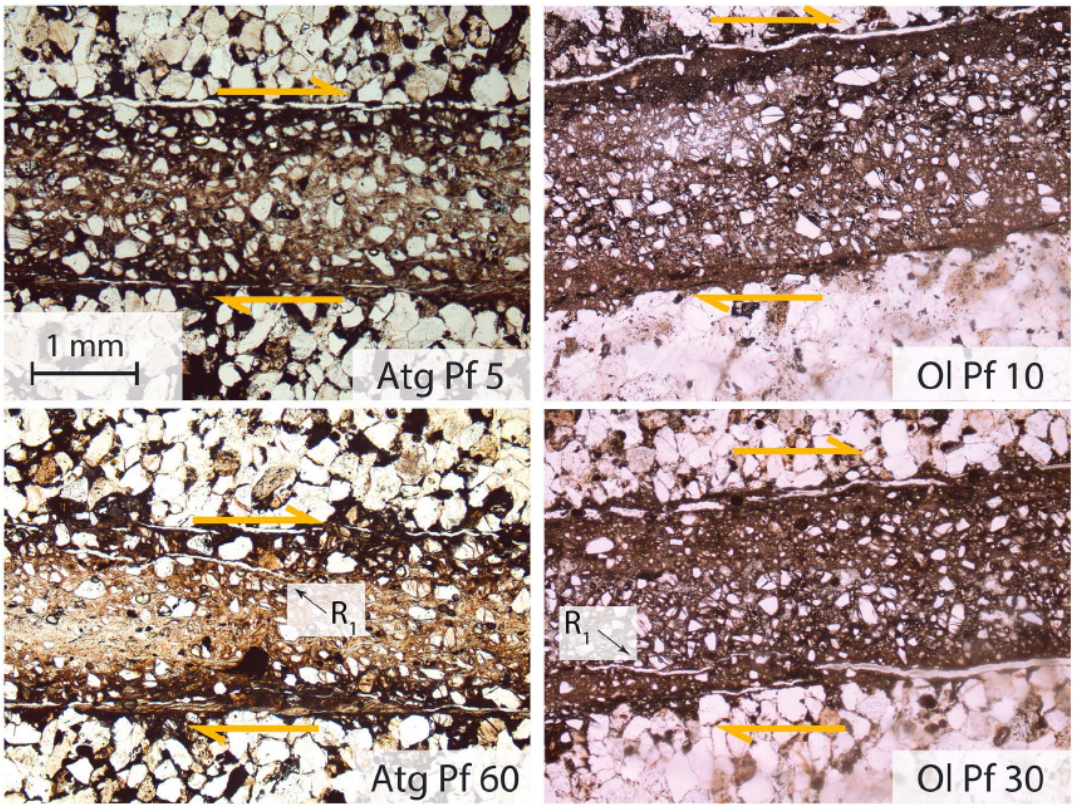

Figure 10. Microstructures of antigorite (Atg) and olivine (Ol) gouges at different pore pressures and effective pressures of 70 MPa. The orange arrow marks the shearing direction.

displacement loading plot (Figures 3a and S1). The yield point is consistent among the same gouge materials at the same controlled effective pressures in Figures 3a and S1, demonstrating that the α value is around 1 in our experiments.

Based on the observations, we propose that the processes associated with compaction are suppressed and dilatant processes are enhanced with increasing pore pressure. Specifically, the decrease in pressurization rate with increasing pore pressure demonstrates that the deformation changes from compaction dominated at low P_f to nearly dilation-dominated processes at high P_f. Following a change in slip velocity, compaction cannot proceed indefinitely and ceases once a new steady state friction is achieved following a change in slip velocity. However, because the compaction and dilation take place during the evolution of friction following a change in slip velocity, we expect the competition to affect the value of the new steady state friction and rate parameters (a-b).

4.3. Pore Pressure Dependence of (a-b)

Given the evidence for decreasing net compaction with increasing pore pressure, we propose that the correlation between pore pressure and (a-b) can be explained by a dilatant hardening mechanism that occurs on a local scale despite the fact that net volume changes are compactions. Because the (a-b) measurements discussed here are all taken from CPP experiments, where velocity steps are between 0.1 and 1 μm/s, the (a-b) dependence on pore pressure from this experiment is not affected by the undrained conditions. When dilation takes place locally during deformation, the transient effective normal stress increases and may approach the total normal stress, which causes frictional strengthening (Marone, 1998). By keeping the applied effective pressure constant, the local normal stress that can be achieved is higher in samples under higher applied pore pressures. In other words, a higher pore pressure could lead to greater frictional strengthening due to local dilatant hardening under net compactive deformation. In this case, the (a-b) that

we reported is an apparent rate dependence of the gouge, because it includes both inherent material properties and evolving fluid pressure, despite the fact that slip velocities are predicted to result in drained behavior based on macroscopic estimates.

This conceptual model for local dilation and transiently increased local normal stress can explain the different degrees of velocity strengthening behaviors observed in gouges of different composition. Lower permeability gouges would be more likely to hinder draining of transient changes in pore fluid pressure and thus cause greater apparent strengthening compared to higher permeability gouges. The fact that the correlation between pore pressure and (a-b) is greater in phyllosilicate gouges is consistent with experimental observations which show that phyllosilicate gouges have low permeability, which would promote undrained behavior (Faulkner & Rutter, 1998; Zhang et al., 1999, 2001). This is also consistent with other studies that show quartz-rich gouges can maintain a high permeability, which would limit pore fluid pressurization (Ikari et al., 2009; Samuelson et al., 2009).

The pore volume measurements during CPP tests corroborate the observed pore fluid pressure dependence of (a-b). The CPP tests demonstrate that less total compaction, which we infer reflects more local dilation, occurs at higher pore pressures (Figure 7). More local dilation corresponds to greater local hardening effects and is consistent with the larger increase on (a-b) of all gouges with higher pore fluid pressures.

The decrease in fluid pressurization with increasing slip velocity in the CPV tests can be explained by the effect of slip velocity on dilation. As slip velocity increases, the amount of local dilation increases and compensates for the compaction, leading to a decrease in the pressurization rate of the pore fluid. This effect of slip velocity on dilation has also been shown by previous studies where the net volume changes are dilatant (e.g., Morrow & Byerlee, 1989). This stands true for all of the gouge compositions that we tested, although the largest effect is seen during deformation of antigorite.

The fact that antigorite shows the greatest change in the pressurization rate with increasing pore pressure conditions is consistent with it also exhibiting the more significant increase in (a-b) with increasing pore pressure. We interpret that the presence of R_1 shear fractures in gouge deformed at higher pore pressures could also contribute to higher amount of dilation leading to greater dilatant hardening given the fact that these features are only observed at higher pore pressure where the mechanical data show evidence for lower net compaction. We also posit that the more extensive grain size reduction distributed over a thicker zone, as observed in samples deformed at higher pore pressure, could tend to enhance local dilation through the associated cracking (Figure 11) and led to the apparent increase of (a-b) in the gouges.

The effect of dilatant hardening on gouge deformation has been observed in previous studies. Ikari et al. (2009) suggested that a low pore pressure could reduce the potential for velocity strengthening because compaction by consolidation and cementation is favored at low pore pressure. However, this is discussed in a context of the effect of high effective pressure at low pore pressure conditions. Our observations suggest that dilation may also be affected by the absolute pore pressure level where dilation increases as the pore pressure level becomes elevated. French and Zhu (2017) have found that high pore pressure impedes the rate of fault propagation during the loss of cohesion in serpentinite and leads to strengthening of the material and more stable failure. The results from this study demonstrated that dilatant hardening could also have a significant effect on the frictional deformation of gouge materials and lead to an apparent velocity strengthening that correlates with pore pressure magnitude.

4.4. Characteristic Displacement (D_c)

The characteristic displacement of antigorite is ~5 times larger than any of other gouge materials that we tested. In the critical stiffness friction stability criterion, larger D_c would lead to a lower critical stiffness of the antigorite gouge and therefore favor more stable slip. This suggests that the slip of antigorite is more likely to favors slow slip than all other materials studied here under room temperature conditions.

For antigorite friction, higher pore pressure also leads to an increase in the characteristic displacement (Figure 6b). This observation is consistent with the discovery of French and Zhu (2017), who suggested that the dilatancy hardening causes an increase in the slip weakening distance. Increase in D_c would reduce the critical stiffness and, therefore, favor stable sliding. The parameter D_c has been correlated with the thickness of the zone of localized shear strain (Marone & Kilgore, 1993). The thicker zone of comminution observed in

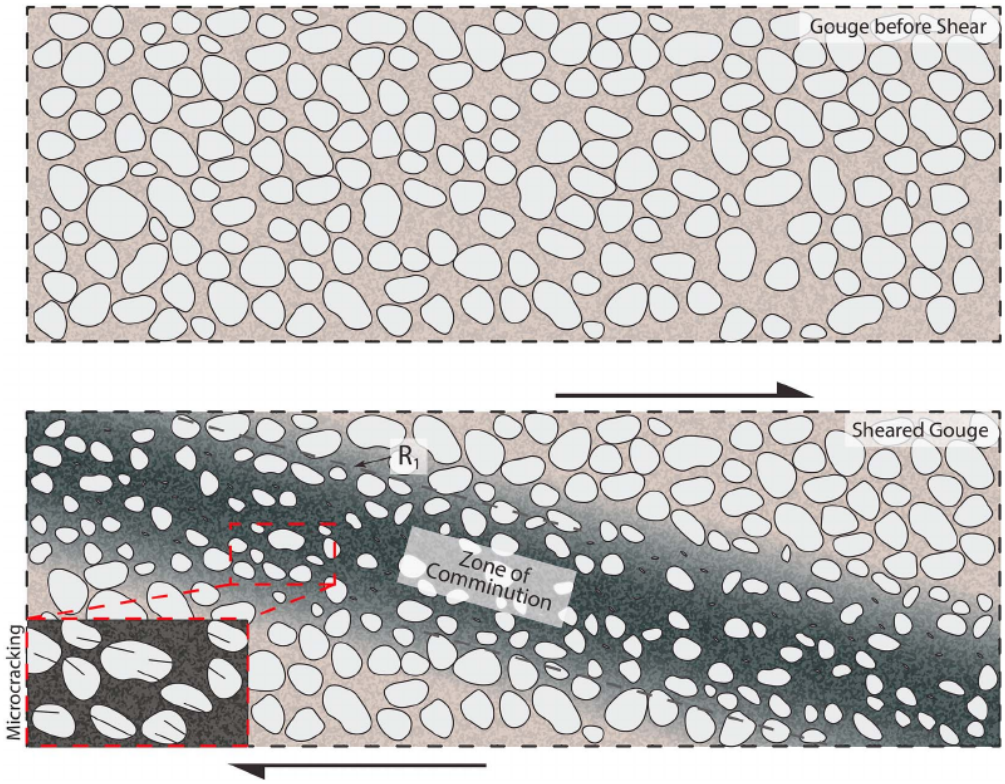

Figure 11. An illustration of the structures seen in the gouges. The shearing results in the development of comminution zone with grain size reduction and R_1 Riedel fracture. At grain scale, development of microcracks promotes the grain size reduction processes.

thin sections of gouge deformed at high pore pressures also seems to support a more distributed zone of deformation (Figure 10). Thus, these results suggest that distributed deformation would favor a more stable slip compared to localized deformation. This is also consistent with our observation that (a-b) increases with increasing pore pressure.

4.5. Slow Slip in Serpentine

The observed dependence of rate and state friction parameters on pore fluid pressure suggests that in addition to the inherent material properties, local dilatant hardening in gouge materials could potentially lead to slow slip (Segall et al., 2010). From the observations of this study, the largest effect of local dilation is documented during deformation of antigorite. It is reasonable to infer that the frictional deformation characteristics of antigorite are the most likely to produce slow slip of the gouges that we tested. We propose that slip that occurs in regions with a large presence of the antigorite or gouge with similar frictional properties and high pore pressure would likely favor slow slip.

The strengthening effect of a dilatant hardening mechanism has been discussed in several studies (Brace & Bombolakis, 1963; French & Zhu, 2017; Rudnicki & Chen, 1988). However, our study shows that it is necessary to consider the absolute level of pore pressure especially when pore pressure is high. The enhanced rate strengthening of friction could come from both effective pressure reduction and pore pressure increase. For antigorite gouges, the high pore pressure could cause a transition in the frictional behavior from unstable to stable slip. This observation is especially important in regions such as subduction zones, transform faults, and mid-ocean ridges where large amounts of fluid are brought to the fault zone to induce extensive serpentinization. Although our experiments are all conducted at room temperature, the findings of this study also seem to be valid at high temperature conditions. Takahashi et al. (2011) observed stick-slip behavior in serpentine at ~500 °C. Interestingly, Okazaki and Katayama (2015) found slow slip in serpentine at above 500 °C and argued that dehydration in serpentine was responsible for the observed slow slip. It is

plausible, that the slow slip is linked to the elevated pore pressure produced by serpentine dehydration at higher temperature. This implies that our observation that high pore pressure promotes slow slip could also apply to high temperature conditions. French and Zhu (2017) found that high pore fluid pressure has a stabilizing effect on fault propagation from 23 to 150 °C. These findings suggest that the strengthening effect of pore fluid pressure observed in this study may be applicable to high temperature conditions as well.

5. Conclusions

Based on the observations in this study, we have found that

1. Chrysotile, olivine, and quartz are velocity strengthening at the conditions of this study and have a similar velocity dependence (a-b), while antigorite is velocity weakening.
2. Increasing pore fluid pressure leads to an increase in (a-b) for all gouge compositions with the largest effect seen in antigorite.
3. At the same effective pressure, the net pore volume reduction during shear diminishes at high pore fluid pressures, indicating less compaction and/or more local dilation at these conditions.
4. The observed correlation between high pore pressure and the magnitude of (a-b) can be explained by dilatant hardening mechanism.
5. Under the same effective pressure conditions, increasing pore pressure would likely lead to a transition in friction from velocity-weakening to velocity strengthening; and lead to evolution of friction parameters, reducing the critical stiffness of the deforming gouge and favors transitional slip behaviors such as slow slips and tremors.

The experimental results of this study demonstrate that high pore pressure can promote an increase in the apparent velocity dependence of gouge and can cause a change in the frictional behavior from velocity weakening to apparent velocity strengthening. This could potentially result in a transition from seismic slip to aseismic creep fault behavior. The results suggest that the presence of high pore pressure may rest the stick-slip earthquakes and cause transitional slip behavior to occur. This study sheds light on the importance of taking into the account the magnitude of fluid pressure when discussing fault slip behavior. It is likely that other minerals also exhibit a correlation between the apparent rate dependence and fluid pressure. This remain to be tested through further extensive study on other materials.

Appendix A

A1. Seal Friction Correction

The axial load (differential stress) applied to the sample is measured with an external load cell and used to determine differential stress. When the load cell is located outside the vessel, some of the measured force is resisted by the friction between the advancing piston and confining pressure seal assembly. Therefore, it is necessary to correct the differential stress by subtracting seal friction.

Seal friction can be determined by first advancing the piston at a constant rate (i.e., 10 μm/s) until it makes contact with the sample. Then the piston is retracted with a rate one order of magnitude lower than the advancing rate (i.e., 1 μm/s) until the differential stress is fully released and becomes constant again. The seal friction is the difference between the two constant stresses at each stable state.

Because the piston is only moving in one direction during the deformation, the true differential stress reading should be Axial load–P_c–Seal Friction.

A2. Contact Offset Correction

As the experiments are conducted on saw cut samples, increasing slip on the surfaces would cause a decrease in the overlapping area. This would make the true differential stress values higher than the measurements read from the force gauge. Following the calculation of Tembe et al. (2010), the area correction would result in 23% stress adjustment by 8 mm of axial shortening. Therefore, a geometric factor A/A_0 is used for this correction (Scott et al., 1994):

$$\frac{A}{A_0} = \frac{\Theta - \sin\Theta}{\pi} \tag{A1}$$

$$\Theta = \pi - 2\sin^{-1}\left(\frac{dl}{2r}\tan\left(\frac{\phi\pi}{180}\right)\right) \tag{A2}$$

where A_0 and A are the original and corrected cross-sectional area of the sample, respectively, Θ is the angle subtended by the point of intersection of two overlapping circles, at the centers of the circles, dl is the axial displacement measured by the LVDTs, and r is the radius of the sample. The corrected differential stress ($\Delta\sigma_{cor}$) is as follows:

$$\Delta\sigma_{cor} = \Delta\sigma\frac{A_0}{A} \tag{A3}$$

A3. Rate-and-State Friction Parameters

Figure A1 illustrates the measurement of characteristic displacement D_c based on the calculation from the friction coefficient. Following a change in slip velocity (V_1 to V_2), the friction coefficient evolves from one steady state (μ_1) to the next steady state (μ_2). The D_c describes the displacement required for the friction coefficient to evolve.

The velocity-dependence factor is calculated based on the equation:

$$a - b = \frac{\mu_1 - \mu_2}{\ln(V_2/V_1)} \tag{A3}$$

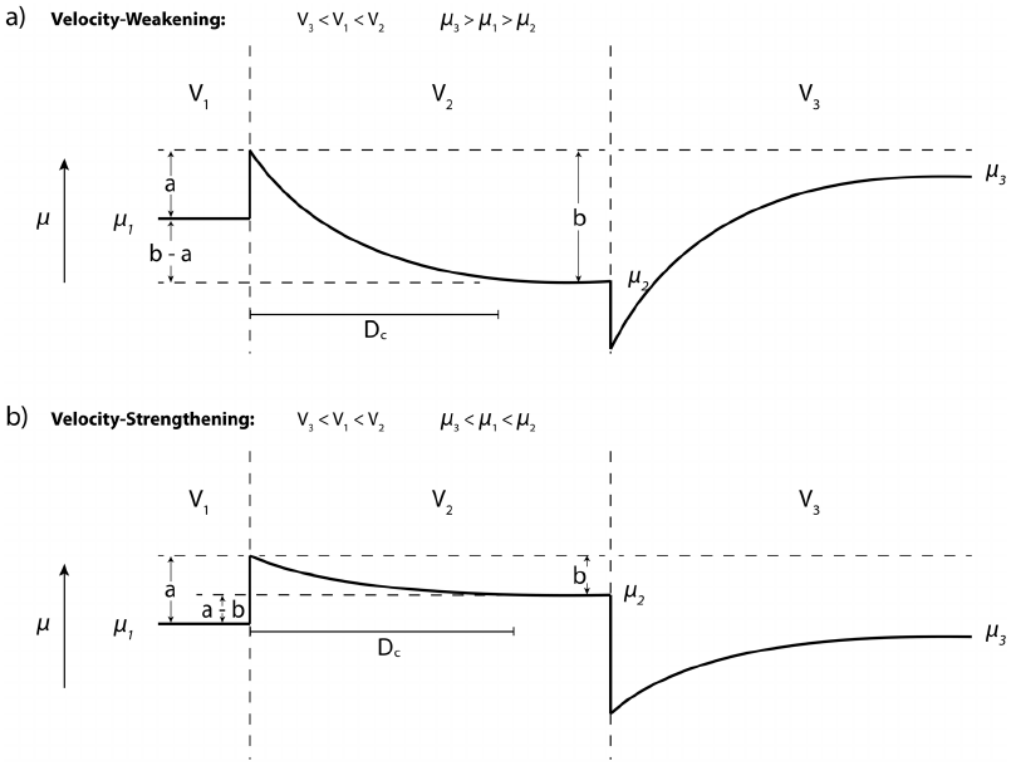

Figure A1. Friction responses to changes in slip velocity. (a) Velocity weakening behavior where increase in slip velocity is associated with a decrease in the friction coefficient (negative *a*-*b*). (b) Velocity strengthening behavior where increase in slip velocity is associated with an increase in the friction coefficient (positive *a*-*b*). The characteristic displacement (D_c) is marked by the distance required for the friction coefficient to evolve to one steady state to the next steady state following a change in slip velocity.

This is derived from constitutive rate-and-state friction laws which describe the dependence of the dynamic friction coefficient on sliding velocity and history (Dieterich, 1979; Ruina, 1983):

$$\mu_s = \mu_1 + a\ln\left(\frac{V_2}{V_1}\right) + b\ln\left(\frac{V_1\theta}{D_c}\right) \tag{A5}$$

$$\frac{d\theta}{dt} = 1 - \frac{\theta V}{D_c} \tag{A6}$$

$$\mu_s = \mu_1 + (a-b)\ln\left(\frac{V_2}{V_1}\right) \tag{A7}$$

where μ_1 is the steady state friction coefficient and μ_s is the dynamic friction coefficient at slip velocity of V_1 and V_2 respectively, a and b are material properties, D_c is the displacement over which friction evolves with slip, and θ is the state variable.

D_c describes the displacement over which friction evolves into 1/e of the change in steady state friction, (i.e., when μ changes to level of b/e; Kilgore et al., 1993). In this study, the D_c is estimated as (1-1/e) of the displacement for friction coefficient to evolve from one steady state to the next steady state where b value is high and cannot be ignored. In cases of olivine, quartz, and chrysotile friction, the b value is small. Therefore, b/e is close to zero. The D_c is then approximated as the displacement for friction coefficient to evolve from one steady state to the next steady state.

Acknowledgments
The authors declare that they have no conflict of interest. The underlying data is available at https://doi-org.proxy-um.researchport.umd.edu/10.13016/gosd-zmob. The authors thank André Niemeijer and the anonymous reviewer for their comments and suggestions. We also like to than the Editor Yves Bernabe for his handling of the manuscript. The authors would like to thank Ann G. Wylie for providing the chrysotile samples used in this study. We would also like to thank David A. Lockner for his help in the development of sample configurations and for sharing the knowledge on making the lead jacket used in this study. We thank Hiroko Kitajima for her comments and discussions on the development of this study. This work is supported by the Department of Energy, Office of Science, the Office of Basic Energy Sciences, Chemical Sciences, Geosciences, and Biosciences Division under award no. DE-FG-0207ER15916 and by the National Science Foundation under grant nos. EAR-1761912 and EAR-1452339.

References

Beeler, N. M. (2007). Laboratory-observed faulting in intrinsically and apparently weak materials. *The Seismogenic Zone of Subduction Thrust Faults*, 370–449.
Bilek, S. L., & Lay, T. (2002). Tsunami earthquakes possibly widespread manifestations of frictional conditional stability. *Geophysical Research Letters*, *29*(14), 1673. https://doi.org/10.1029/2002GL015215
Blanpied, M. L., Lockner, D. A., & Byerlee, J. D. (1995). Frictional slip of granite at hydrothermal conditions. *Journal of Geophysical Research - Solid Earth*, *100*(B7), 13,045–13,064. https://doi.org/10.1029/95JB00862
Brace, W. F., & Bombolakis, E. G. (1963). A note on brittle crack growth in compression. *Journal of Geophysical Research*, *68*(12), 3709–3713 . https://doi-org.proxy-um.researchport.umd.edu/10.1029/JZ068i012p03709
Byerlee, J. D. (1978). Friction of rocks. *Pure and Applied Geophysics PAGEOPH*, *116*(4–5), 615–626. https://doi-org.proxy-um.researchport.umd.edu/
Carpenter, B. M., Collettini, C., Viti, C., & Cavallo, A. (2016). The influence of normal stress and sliding velocity on the frictional behaviour of calcite at room temperature: Insights from laboratory experiments and microstructural observations. *Geophysical Journal International*, *205*(1), 548–561. https://doi-org.proxy-um.researchport.umd.edu/10.1093/gji/ggw038
Chen, J., Niemeijer, A. R., & Spiers, C. J. (2017). Microphysically derived expressions for rate-and-state friction parameters, a, b, and D_c. *Journal of Geophysical Research: Solid Earth*, *122*, 9627–9657. https://doi-org.proxy-um.researchport.umd.edu/10.1002/2017JB014226
Chernak, L. J., & Hirth, G. (2010). Deformation of antigorite serpentinite at high temperature and pressure. *Earth and Planetary Science Letters*, *296*(1–2), 23–33. https://doi-org.proxy-um.researchport.umd.edu/10.1016/j.epsl.2010.04.035
Chester, F. M. (1994). Effects of temperature on friction: Constitutive equations and experiments with quartz gouge. *Journal of Geophysical Research*, *99*(B4), 7247–7261. https://doi.org/10.1029/93JB03110
Chester, F. M., & Higgs, N. G. (1992). Multimechanism friction constitutive model for ultrafine quartz gouge at hypocentral conditions. *Journal of Geophysical Research*, *97*(B2), 1859–1870. https://doi-org.proxy-um.researchport.umd.edu/10.1029/91JB02349
den Hartog, S. A. M., Saffer, D. M., & Spiers, C. J. (2014). The roles of quartz and water in controlling unstable slip in phyllosilicate-rich megathrust fault gouges. *Earth, Planets and Space*, *66*(1), 1–9. https://doi-org.proxy-um.researchport.umd.edu/10.1186/1880-5981-66-78
den Hartog, S. A. M., & Spiers, C. J. (2013). Influence of subduction zone conditions and gouge composition on frictional slip stability of megathrust faults. *Tectonophysics*, *600*, 75–90. https://doi-org.proxy-um.researchport.umd.edu/10.1016/j.tecto.2012.11.006
Dieterich, J. H. (1979). Modeling of rock friction: 1. Experimental results and constitutive equations. *Journal of Geophysical Research*, *84*(B5), 2161. https://doi.org/10.1029/JB084iB05p02161
Dieterich, J. H., & Conrad, G. (1984). Effect of humidity on time- and velocity-dependent friction in rocks. *Journal of Geophysical Research - Solid Earth*, *89*(B6), 4196–4202. https://doi-org.proxy-um.researchport.umd.edu/10.1029/JB089iB06p04196
Escartín, J., Hirth, G., & Evans, B. (1997). Nondilatant brittle deformation of serpentinites: Implications for Mohr-Coulomb theory and the strength of faults. *Journal of Geophysical Research - Solid Earth*, *102*(B2), 2897–2913. https://doi.org/10.1029/96JB02792
Faulkner, D., & Rutter, E. H. (1998). The gas permeability of clay-bearing fault gouge at 20 °C. *Geological Society of London, Special Publication*, *147*(1), 147–156. https://doi.org/10.1144/GSL.SP.1998.147.01.10
Faulkner, D., & Rutter, E. H. (2003). The effect of temperature, the nature of the pore fluid, and subyield differential stress on the permeability of phyllosilicate-rich fault gouge. *Journal of Geophysical Research - Solid Earth*, *108*(B5), 2227. https://doi-org.proxy-um.researchport.um
2001JB001581
Faulkner, D., Sanchez-Roa, C., Boulton, C., & den Hartog, S. A. M. (2018). Pore fluid pressure development in compacting fault gouge in theory, experiments, and nature. *Journal of Geophysical Research: Solid Earth*, *123*, 226–241. https://doi.org/10.1002/2017JB015130
Fine, R. A., & Millero, F. J. (1973). Compressibility of water as a function of temperature and pressure. *The Journal of Chemical Physics*, *59*(10), 5529–5536. https://doi-org.proxy-um.researchport.umd.edu/10.1063/1.1679903
Frank, F. C. (1965). On dilatancy in relation to seismic sources. *Reviews of Geophysics*, *3*(4), 485. https://doi-org.proxy-um.researchport.umd.edu/10.10
French, M. E., Chester, F. M., & Chester, J. S. (2015). Micromechanisms of creep in clay-rich gouge from the Central Deforming Zone of the San Andreas Fault. *Journal of Geophysical Research: Solid Earth*, *120*, 827–849. https://doi-org.proxy-um.researchport.umd.edu/10.1002/2014JB01

French, M. E., & Zhu, W. (2017). Slow fault propagation in serpentinite under conditions of high pore fluid pressure. *Earth and Planetary Science Letters*, *473*, 131–140. https://doi.org/10.1016/j.epsl.2017.06.009
French, M. E., Zhu, W., & Banker, J. (2016). Fault slip controlled by stress path and fluid pressurization rate. *Geophysical Research Letters*, *43*, 4330–4339. https://doi.org/10.1002/2016GL068893
Goldsby, D. L., & Tullis, T. E. (2002). Low frictional strength of quartz rocks at subseismic slip rates. *Geophysical Research Letters*, *29*(17), 1844. https://doi-org.proxy-um.researchport.umd.edu/10.1029/2002GL015240
Gu, J.-C., Rice, J. R., Ruina, A. L., & Tse, S. T. (1984). Slip motion and stability of a single degree of freedom elastic system with rate and state dependent friction. *Journal of the Mechanics and Physics of Solids*, *32*(3), 167–196. https://doi-org.proxy-um.researchport.umd.edu/10.1016/0022-5
Heise, W., Caldwell, T. G., Bannister, S., Bertrand, E. A., Ogawa, Y., Bennie, S. L., & Ichihara, H. (2017). Mapping subduction interface coupling using magnetotellurics: Hikurangi margin, New Zealand. *Geophysical Research Letters*, *44*, 9261–9266. https://doi.org/10.1002/2017GL074641
Heise, W., Caldwell, T. G., Bertrand, E. A., Hill, G. J., Bennie, S. L., & Ogawa, Y. (2013). Changes in electrical resistivity track changes in tectonic plate coupling. *Geophysical Research Letters*, *40*, 5029–5033. https://doi-org.proxy-um.researchport.umd.edu/10.1002/grl.50959
Ikari, M. J., Marone, C., & Saffer, D. M. (2011). On the relation between fault strength and frictional stability. *Geology*, *39*(1), 83–86. https://doi.org/10.1130/G31416.1
Ikari, M. J., Saffer, D. M., & Marone, C. (2009). Frictional and hydrologic properties of clay-rich fault gouge. *Journal of Geophysical Research - Solid Earth*, *114*, B05409. https://doi-org.proxy-um.researchport.umd.edu/10.1029/2008JB006089
Kilgore, B. D., Blanpied, M. L., & Dieterich, J. H. (1993). Velocity dependent friction of granite over a wide range of conditions. *Geophysical Research Letters*, *20*(10), 903–906. https://doi-org.proxy-um.researchport.umd.edu/10.1029/93GL00368
Kodaira, S., Iidaka, T., Kato, A., Park, J. O., Iwasaki, T., & Kaneda, Y. (2004). High pore fluid pressure may cause silent slip in the Nankai Trough. *Science*, *304*(5675), 1295–1298. https://doi-org.proxy-um.researchport.umd.edu/10.1126/science.1096535
Leeman, J. R., Saffer, D. M., Scuderi, M. M., & Marone, C. (2016). Laboratory observations of slow earthquakes and the spectrum of tectonic fault slip modes. *Nature Communications*, *7*(1), 11104. https://doi-org.proxy-um.researchport.umd.edu/10.1038/ncomms11104
Lockner, D. A., Summers, R., & Byerlee, J. D. (1986). Effects of temperature and sliding rate on frictional strength of granite. *Pure and Applied Geophysics PAGEOPH*,*124*(3), 445–469. https://doi-org.proxy-um.researchport.umd.edu/10.1007/BF00877211
Logan, J. M., Dengo, C. A., Higgs, N. G., & Wang, Z. Z. (1992). Fabrics of experimental fault zones: Their development and relationship to mechanical behavior. *International Geophysics*, *51*(C), 33–67. https://doi-org.proxy-um.researchport.umd.edu/10.1016/S0074-6142(08)62814-4
Marone, C. (1998). Laboratory-derived friction laws and their application to seismic faulting. *Annual Review of Earth and Planetary Sciences*, *26*(1), 643–696. https://doi-org.proxy-um.researchport.umd.edu/10.1146/annurev.earth.26.1.643
Marone, C., & Kilgore, B. (1993). Scaling of the critical slip distance for seismic faulting with shear strain in fault zones. *Nature*, *362*(6421), 618–621. https://doi-org.proxy-um.researchport.umd.edu/10.1038/362618a0
Moore, D. E., & Lockner, D. A. (2011). Frictional strengths of talc-serpentine and talc-quartz mixtures. *Journal of Geophysical Research - Solid Earth*, *116*, B01403. https://doi.org/10.1029/2010JB007881
Moore, D. E., Lockner, D. A., Summers, R., Ma, S., & Byerlee, J. D. (1996). Strength of crisolite-serpentinite gouge under hydrothermal conditions: Can it explain a weak San Andreas fault? *Geology*, *24*(11), 1041–1044. https://doi-org.proxy-um.researchport.umd.edu/10.1130/0091-7
Moore, D. E., Lockner, D. A., Tanaka, H., & Iwata, K. (2004). The coefficient of friction of chrysotile gouge at seismogenic depths. *International Geology Review*, *46*(5), 385–398. https://doi-org.proxy-um.researchport.umd.edu/10.2747/0020-6814.46.5.385
Morrow, C. A., & Byerlee, J. D. (1989). Experimental studies of compaction and dilatancy during frictional sliding on faults containing gouge. *Journal of Structural Geology*, *11*(7), 815–825. https://doi-org.proxy-um.researchport.umd.edu/10.1016/0191-8141(89)90100-4
Morrow, C. A., Radney, B., & Byerlee, J. D. (1992). Frictional strength and the effective pressure law of montmorillonite and lllite clays. *International Geophysics*, *51*, 69–88. https://doi-org.proxy-um.researchport.umd.edu/10.1016/S0074-6142(08)62815-6
Morrow, C. A., Shi, L. Q., & Byerlee, J. D. (1984). Permeability of fault gouge under confining pressure and shear stress. *Journal of Geophysical Research*, *89*(B5), 3193–3200. https://doi-org.proxy-um.researchport.umd.edu/10.1029/JB089iB05p03193
Niemeijer, A., & Collettini, C. (2013). Frictional properties of a low-angle normal fault under in situ conditions: Thermally-activated velocity weakening. *Pure and Applied Geophysics*, *171*(10), 2641–2664. https://doi-org.proxy-um.researchport.umd.edu/10.1007/s00024-013-0759-6
Niemeijer, A., Marone, C., & Elsworth, D. (2010). Frictional strength and strain weakening in simulated fault gouge: Competition between geometrical weakening and chemical strengthening. *Journal of Geophysical Research - Solid Earth*, *115*, B10207. https://doi.org/10.1029/2009JB000838
Okazaki, K., & Katayama, I. (2015). Slow stick slip of antigorite serpentinite under hydrothermal conditions as a possible mechanism for slow earthquakes. *Geophysical Research Letters*, *42*, 1099–1104. https://doi.org/10.1002/2014GL062735
Ougier-Simonin, A., & Zhu, W. (2013). Effects of pore fluid pressure on slip behaviors: An experimental study. *Geophysical Research Letters*, *40*, 2619–2624. https://doi.org/10.1002/grl.50543
Ougier-Simonin, A., & Zhu, W. (2015). Effect of pore pressure buildup on slowness of rupture propagation. *Journal of Geophysical Research: Solid Earth*, *120*, 7966–7985. https://doi.org/10.1002/2015JB012047
Peacock, S. M., Christensen, N. I., Bostock, M. G., & Audet, P. (2011). High pore pressures and porosity at 35 km depth in the Cascadia subduction zone. *Geology*, *39*(5), 471–474. https://doi-org.proxy-um.researchport.umd.edu/10.1130/G31649.1
Peng, Z., & Gomberg, J. (2010). An integrated perspective of the continuum between earthquakes and slow-slip phenomena. *Nature Geoscience*, *3*(9), 599–607. https://doi.org/10.1038/ngeo940
Proctor, B. P., Mitchell, T. M., Hirth, G., Goldsby, D. L., Zorzi, F., Platt, J. D., & Di Toro, G. (2014). Dynamic weakening of serpentinite gouges and bare surfaces at seismic slip rates. *Journal of Geophysical Research: Solid Earth*, *119*, 8107–8131. https://doi-org.proxy-um.researchport 2014JB011057
Rabinowicz, E. (1958). The intrinsic variables affecting the stick-slip process. *Proceedings of the Physical Society*, *71*(4), 668–675. https://doi.org/10.1088/0370-1328/71/4/316
Rathbun, A. P., & Marone, C. (2013). Symmetry and the critical slip distance in rate and state friction laws. *Journal of Geophysical Research: Solid Earth*, *118*, 3728–3741. https://doi-org.proxy-um.researchport.umd.edu/10.1002/jgrb.50224
Reinen, L. A., Weeks, J. D., & Tullis, T. E. (1994). The frictional behavior of lizardite and antigorite serpentinites: Experiments, constitutive models, and implications for natural faults. *Pure and Applied Geophysics PAGEOPH*, *143*(1–3), 317–358. https://doi-org.proxy-um.researchport.um BF00874334
Rice, J. R. (1975). On the stability of dilatant hardening for saturated rock masses. *Journal of Geophysical Research*, *80*(11), 1531–1536. https://doi-org.proxy-um.researchport.umd.edu/10.1029/JB080i011p01531
Rice, J. R., & Ruina, A. L. (1983). Stability of steady frictional slipping. *Journal of Applied Mechanics*, *50*(2), 343. https://doi-org.proxy-um.researchpo 1.3167042

Rubin, A. M. (2008). Episodic slow slip events and rate-and-state friction. *Journal of Geophysical Research - Solid Earth*, *113*, B11414. https://doi-org.proxy-um.researchport.umd.edu/10.1029/2008JB005642

Rudnicki, J. W., & Chen, C. H. (1988). Stabilization of rapid frictional slip on a weakening fault by dilatant hardening. *Journal of Geophysical Research*, *93*(B5), 4745–4757. https://doi-org.proxy-um.researchport.umd.edu/10.1029/JB093iB05p04745

Ruina, A. (1983). Slip instability and state variable friction laws. *Journal of Geophysical Research - Solid Earth*, *88*(B12), 10359–10370. https://doi-org.proxy-um.researchport.umd.edu/10.1029/JB088iB12p10359

Rutter, E. H., & Hackston, A. (2017). On the effective stress law for rock-on-rock frictional sliding, and fault slip triggered by means of fluid injection. *Philosophical Transactions of the Royal Society A: Mathematical, Physical and Engineering Sciences*, *375*(2103), 20160001. https://doi-org.proxy-um.researchport.umd.edu/10.1098/rsta.2016.0001

Samuelson, J., Elsworth, D., & Marone, C. (2009). Shear-induced dilatancy of fluid-saturated faults: Experiment and theory. *Journal of Geophysical Research - Solid Earth*, *114*, B12404. https://doi-org.proxy-um.researchport.umd.edu/10.1029/2008JB006273

Sawai, M., Niemeijer, A., Plümper, O., Hirose, T., & Spiers, C. J. (2016). Nucleation of frictional instability caused by fluid pressurization in subducted blueschist. *Geophysical Research Letters*, *43*, 2543–2551. https://doi-org.proxy-um.researchport.umd.edu/10.1002/2015GL067569

Scott, D. R., Lockner, D. A., Byerlee, J. D., & Sammis, C. G. (1994). Triaxial testing of Lopez Fault gouge at 150 MPa mean effective stress. *Pure and Applied Geophysics PAGEOPH*, *142*(3–4), 749–775. https://doi-org.proxy-um.researchport.umd.edu/10.1007/BF00876063

Scuderi, M. M., Collettini, C., & Marone, C. (2017). Frictional stability and earthquake triggering during fluid pressure stimulation of an experimental fault. *Earth and Planetary Science Letters*, *477*, 84–96. https://doi-org.proxy-um.researchport.umd.edu/10.1016/j.epsl.2017.08.009

Segall, P., Rubin, A. M., Bradley, A. M., & Rice, J. R. (2010). Dilatant strengthening as a mechanism for slow slip events. *Journal of Geophysical Research - Solid Earth*, *115*, B12305. https://doi-org.proxy-um.researchport.umd.edu/10.1029/2010JB007449

Shelly, D. R. (2010). Migrating tremors illuminate complex deformation beneath the seismogenic San Andreas fault. *Nature*, *463*(7281), 648–652. https://doi-org.proxy-um.researchport.umd.edu/10.1038/nature08755

Shelly, D. R., Beroza, G. C., Ide, S., & Nakamula, S. (2006). Low-frequency earthquakes in Shikoku, Japan, and their relationship to episodic tremor and slip. *Nature*, *442*(7099), 188–191. https://doi.org/10.1038/nature04931

Takahashi, M., Uehara, S. I., Mizoguchi, K., Shimizu, I., Okazaki, K., & Masuda, K. (2011). On the transient response of serpentine (antigorite) gouge to stepwise changes in slip velocity under high-temperature conditions. *Journal of Geophysical Research - Solid Earth*, *116*, B10405. https://doi-org.proxy-um.researchport.umd.edu/10.1029/2010JB008062

Tembe, S., Lockner, D. A., & Wong, T. (2010). Effect of clay content and mineralogy on frictional sliding behavior of simulated gouges: Binary and ternary mixtures of quartz, illite, and montmorillonite. *Journal of Geophysical Research - Solid Earth*, *115*, B03416. https://doi.org/10.1029/2009JB006383

Terzaghi, K. (1943). *Theoretical soil mechanics*. London: Chapman and Hall, Limited. https://doi-org.proxy-um.researchport.umd.edu/10.1002/9780

Verberne, B. A., He, C., & Spiers, C. J. (2010). Frictional properties of sedimentary rocks and natural fault gouge from the Longmen Shan fault zone, Sichuan, China. *Bulletin of the Seismological Society of America*, *100*(5B), 2767–2790. https://doi-org.proxy-um.researchport.umd.edu/10

Zhang, S., Tullis, T. E., & Scruggs, V. J. (1999). Permeability anisotropy and pressure dependency of permeability in experimentally sheared gouge materials. *Journal of Structural Geology*, *21*(7), 795–806. https://doi.org/10.1016/S0191-8141(99)00080-2

Zhang, S., Tullis, T. E., & Scruggs, V. J. (2001). Implications of permeability and its anisotropy in a mica gouge for pore pressures in fault zones. *Tectonophysics*, *335*(1–2), 37–50. https://doi-org.proxy-um.researchport.umd.edu/10.1016/S0040-1951(01)00044-0

Zhu, W., & Wong, T. (1997). The transition from brittle faulting to cataclastic flow: Permeability evolution. *Journal of Geophysical Research - Solid Earth*, *102*(B2), 3027–3041. https://doi-org.proxy-um.researchport.umd.edu/10.1029/96JB03282